ACS OMEGA

http://pubs.acs.org/journal/acsodf

Article

EDA–NOCV Calculation for Efficient N_2 Binding to the Reduced Ni_3S_8 Complex: Estimation of Ni–N_2 Intrinsic Interaction Energies

Sai Manoj N. V. T. Gorantla and Kartik Chandra Mondal*

Cite This: *ACS Omega* 2021, 6, 33389–33397

Read Online

ACCESS | Metrics & More | Article Recommendations | Supporting Information

ABSTRACT: The binding of the dinitrogen molecule to the metal center is the first and crucial step toward dinitrogen activation. Favorable interaction energies are desired by chemists and biochemists to study model complexes in the laboratory. An electrochemically reduced form of a previously isolated sulfur-bridged Ni_3S_8 complex is inferred to bind N_2 at multiple Ni centers, and this bonded N_2 undergoes reductive protonation to produce hydrazine (N_2H_4) as the product in the presence of a proton donor. Density functional theory (DFT) calculations and quantum theory of atoms in molecules (QTAIM) analysis have been carried out to shed light on the nature of N_2 binding to an anionic trinuclear Ni_3S_8 complex. Additionally, energy decomposition analysis with the combination of natural orbital for chemical valence (EDA–NOCV) analysis has been performed to estimate the pairwise interaction energies between the Ni center and the N_2 molecule under experimental conditions.

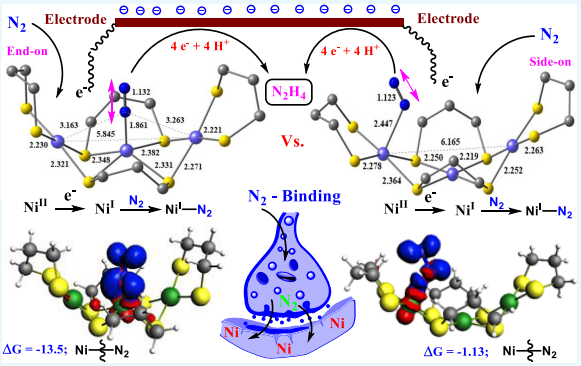

INTRODUCTION

The binding of aerial dinitrogen (N_2) followed by its reduction are some of the most important natural biochemical processes.[1−5] N_2 is the most abundant gas in the earth's atmosphere, accounting for roughly 78% of all components. The respiratory process involves O_2 despite such a high abundance of N_2 in the earth's atmosphere, owing to the kinetic inertness of the N≡N bond. Furthermore, the nonpolar N_2 molecule possesses two deep-lying pairs of electrons (:N≡N:) making N_2 itself a poor donor ligand.[6] Sulfur-bridged molybdenum-iron ($MoFe_7S_9C^{1-}$)-based nitrogenase enzymes (FeMoco) can bind aerial N_2 under a reduced state and catalyze reduction leading to the formation of ammonia.[1−3,5] It should be noted that active binding sites of metalloenzymes Ni-superoxide dismutase[7,8] and Ni–Fe hydrogenase[9,10] possess S-donor bridges. The metal ion-containing inorganic units are well protected by the proteins that surround them to prevent them from undergoing undesired oxidation reactions.[1] Chemists and biochemists have come up with the syntheses, isolations, and characterizations of several model complexes to study their electronic structures and chemical properties under different conditions, including binding with CO and N_2.[11−30] The redox properties have been often studied using cyclic voltammetry. Over the last decade, there has been a significant increase in research efforts focused on N_2 binding at metal (M) centers, followed by activation of the N≡N bond via reductive protonation.[15] Several metal complexes, which possess a bond with N_2 in the reduced oxidation state of M, have been isolated, characterized, and further studied using spectroscopic techniques (M = Fe, Mo, Os, Ru, Re, etc.).[11−18]

The reductive protonation of N_2 can lead to the formation of either ammonia (NH_3) or hydrazine (N_2H_4) or sometimes a mixture of both.[11−30] These reports mostly focus on changes in N–N bond orders, which are computed by estimating Wiberg bond order P(N–N) values to compare them to experimentally determined N–N bond lengths.[15,17,24−26] Authors of these previous reports have often pointed out that π back-donation from metal to N_2 (M → N_2) is crucial for the weakening of the N≡N bond. The reductive electron transfer from external reducing agents to the metal center is very important. The higher the accumulation of electron densities on metal atoms, the higher the π back-donation from metal to N_2 (Scheme 1).[17,24−26] In recent times, there have been several reports on the first-row transition metal-based dinitrogen activation (M = V, Fe, Ni, Co, Ni, Cu).[27] Very recently, N_2 binding has been reported to take place at the electron-deficient boron center of boron-cyclic-alkyl-amino-carbene compounds.[28] Moreover, reductive protonation leading to the formation of NH_3 has been successfully achieved.[28] These boron compounds are highlighted to be equivalent to metal complexes that can perform a similar job.[29] However, there is no report on the estimation of M–N_2 interaction energies

Received: July 14, 2021
Accepted: November 10, 2021
Published: December 2, 2021

Scheme 1. Interacting Orbitals between Metal (M) and N_2

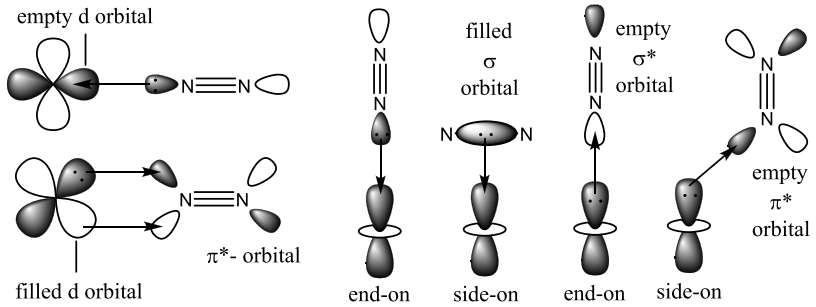

Scheme 2. Proposed Scheme of N_2 Binding to the Ni_3Si_8 Unit of Complex $(LS_2)_4Ni(II)_3^{2-}$[39]

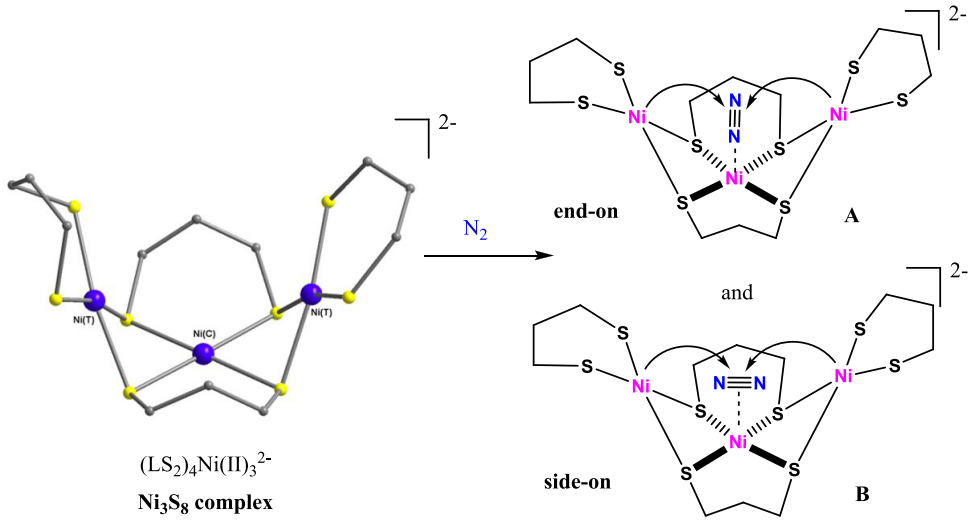

showing the extent of π back-donation from M → N_2 and σ-donation from N_2 → M (M = transition metal).[30] The N≡N bond of the free dinitrogen (N_2) is quite strong. The energy decomposition analysis with the combination of natural orbital for chemical valence (EDA−NOCV) analysis of free N_2 molecule showed that 30% of the total interaction energy between two interacting N atoms is only contributed by electrostatic energy (ΔE_{elstat}) and the remaining 70% is orbital interaction energy (ΔE_{orb}).[6b] The charge separation (q) and dipole moment (μ) are zero. The Pauli repulsion energy (ΔE_{Pauli}) between two interacting N atoms is quite high, preventing the two nuclei from further coming closer (d_{N-N} = 1.102 Å). The Wiberg bond order P(N−N) has been estimated to be 3.03. The orbital interaction energy (ΔE_{orb}) is further split into two parts [for $\sigma(3\sigma_g^+)$ + $\pi(1\pi_u)$ orbitals]. The σ interaction is 65.6% while the π-interaction is nearly half (34.4%). These two interactions (σ + π) combined to give the total orbital interaction energy (ΔE_{orb}).[6b] Most importantly, doubly degenerate π^*-orbitals ($1\pi_g$) of N_2, which are composed of the p_x and p_y atomic orbitals of two interacting N atoms, are quite high in energy ($1\pi_g$; lowest unoccupied molecular orbital (LUMO)). The LUMO + 1 is $3\sigma_u^+$, and the highest occupied molecular orbital (HOMO) is N−N $\sigma(3\sigma_g^+)$ orbital.[6b]

It has been often found that the reductive protonation of $(L_n)M(N_2)$ can lead to the formation of NH_3 or N_2H_4 under mild conditions.[31−34] The latter's enthalpy of formation is known to be endothermic by +159.2 kJ mol^{-1}, whereas that of the former is exothermic. Furthermore, a huge amount of energy is stored in N_2H_4, which can be released by both chemical and electrochemical methods without any energy barrier. Hydrazine is utilized as rocket fuel due to its very high energy storage density [1.5368 × 10^{10} J m^{-3}/4269 Wh L^{-1} (chemical/electrochemical)].[35−37] Recently, an isolated U-shaped dianionic complex $(LS_2)_4Ni(II)_3^{2-}$ (LS_2^{2-} = $^-$S−$(CH_2)_3$−S^-) (abbreviated as Ni_3S_8 complex)[38] has been shown to electrochemically produce hydrazine (N_2H_4) in the presence of PhOH as a proton donor. There is no illustration or research on N_2 binding and its electrochemical reduction processes. Herein, we report density functional theory (DFT), quantum theory of atoms in molecules (QTAIM), and EDA−NOCV calculations[39−48] to shed light on the binding of N_2 at the Ni center. We have further investigated the bonding scenarios and estimated the pairwise interaction energies between the electrochemically reduced (Ni^{II} → Ni^{I}) Ni center and N_2 molecules.

RESULTS AND DISCUSSION

The dianionic complex Ni_3S_8 [$(LS_2)_4Ni(II)_3^{2-}$; (LS_2^{2-} = $^-$S−$(CH_2)_3$−S^-)] has been previously characterized using X-ray single-crystal diffraction.[38] This anionic trinuclear Ni(II)-based complex is composed of three Ni(II) ions and four dianionic S-donor ligands (LS_2^{2-}). The central Ni(II) [Ni^C] is connected to two terminal Ni(II) centers [Ni^T] by four μ−S_L bridges (Scheme 2, left). All three Ni(II) ions have adopted a distorted square planar geometry. The Ni−S bond lengths range from 2.202(3) to 2.265(3) Å. The S−Ni−S angles around the square planar Ni^C center are 78.49/78.55° and 101.17/101.81°

https://doi.org/10.1021/acsomega.1c03715
ACS Omega 2021, 6, 33389−33397

Scheme 3. Structures of Optimized Geometries of Dianionic Singlet (Complex 1) and Trianionic Doublet States with End-On (2) and Side-On (3) Overlap of the $(Ni_3Si_8)N_2$ Complex

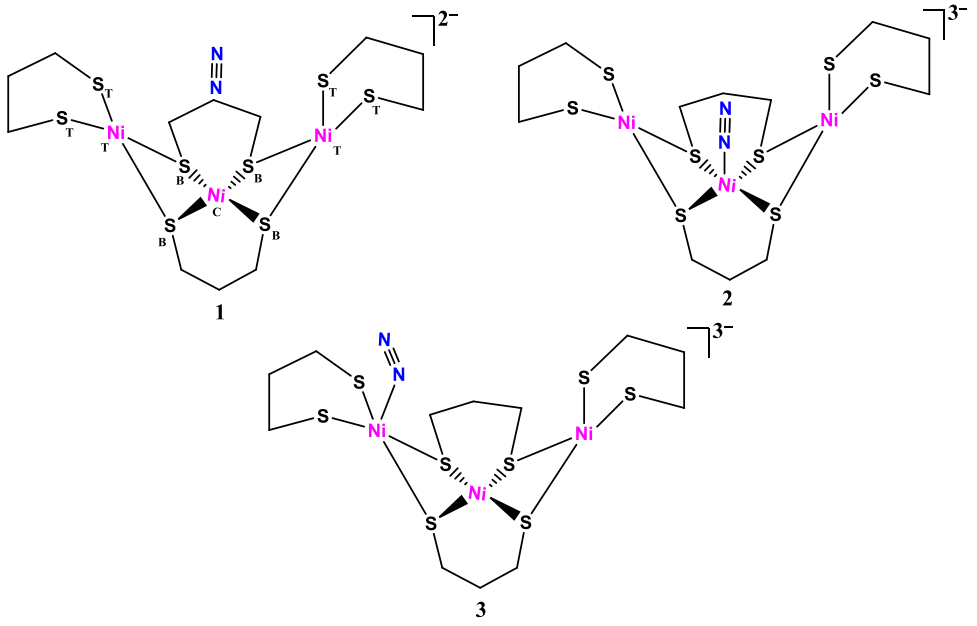

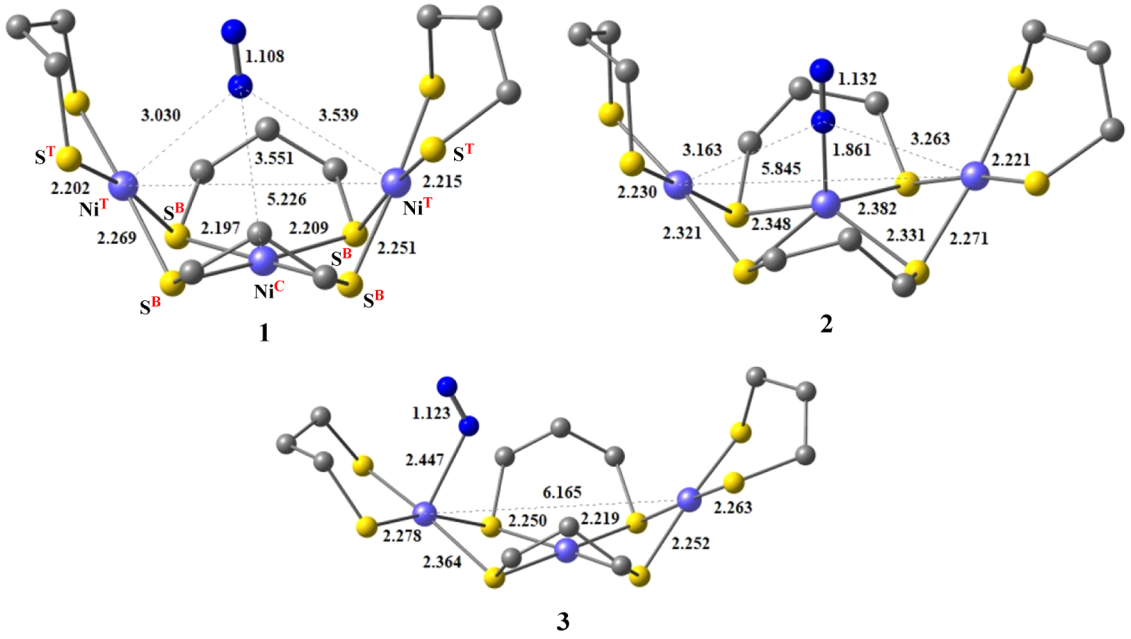

Figure 1. Optimized geometries of dianionic singlet (complex **1**) and trianionic doublet states with end-on (**2**) and side-on (**3**) N_2-bonded $(Ni_3Si_8)N_2$ complexes at the BP86-D3(BJ)/Def2TZVPP level. Wiberg bond order P(N−N) values: 2.95 (**1**), 2.63, (**2**) and 2.79 (**3**).

while the corresponding angles around the two Ni^T centers are 76.16−76.66/93.76−99.22° and 94.86−95.49/92.33−92.68°.[38] The deviation from the regular square planar geometry of central Ni^C is greater than those of terminal Ni^T centers (Scheme 2, left). The Ni^T−Ni^C distances are 2.9161(19)−2.9396(19) Å. The six-membered $(LS_2)Ni(II)$ unit can have different conformations (distorted chair and boat similar to cyclohexane). The cyclic voltammetry (CV) measurement in tetrahydrofuran (THF) showed two reduction processes −2.20 and −2.40 V vs fc^+/fc under both argon and dinitrogen atmospheres in the absence of a proton source, suggesting the reduction of square planar Ni^{II} ion to paramagnetic Ni^I ion $[(LS_2)_4Ni(II)_3^{2-} + e^- \rightarrow (LS_2)_4Ni\text{-}(II)_2Ni(I)^{3-}]$.[38] The electrochemical formation of tetra-anion $[(LS_2)_4Ni(II)_2Ni(I)^{3-} + e^- \rightarrow (LS_2)_4Ni(II)Ni(I)_2^{4-}]$ at −2.40 V cannot be excluded either. Interestingly, these two values are reported to shift to −2.35 and −2.85 V vs fc^+/fc, respectively, under the N_2 atmosphere in the presence of PhOH, suggesting possible H-bonding interactions between H−O_{Ph} and S-atoms of the dianionic complex.[38] However, its mononuclear Ni(II) analogue does not show electrochemical N_2 reduction.[38]

We have performed geometry optimization of the dinitrogen-encapsulated dianionic $(Ni_3S_8)N_2$ complex (**1**) containing three Ni(II) centers in its singlet and triplet states at the BP86-D3(BJ)/Def2TZVPP level of theory [**1** = $(LS_2)_4(N_2)Ni(II)_3^{2-}$; LS_2^{2-} = ^-S−$(CH_2)_3$−S^-] (Schemes 2

https://doi.org/10.1021/acsomega.1c03715
ACS Omega 2021, 6, 33389−33397

and 3). The singlet state of **1** is more stable than its triplet state by 30.3 kcal mol^{-1}. The binding of dinitrogen molecule (N_2) to the trinuclear $(LS_2)_4(N_2)Ni(II)_3^{2-}$ complex in an end-on/side-on fashion to the central Ni and charge donations from the two terminal Ni atoms has been previously shown, as presented in Scheme 2A,B.[38]

We tried to optimize the singlet-state $(LS_2)_4(N_2)Ni(II)_3^{2-}$ in end-on (**A**) and side-on (**B**) fashions as shown in Scheme 2. Eventually, the side-on (**B**) input geometry led to optimization in the end-on mode (**A**). We further performed the geometry optimization of the singlet state in an end-on and side-on fashion at the M06-2x-D3 level using the Def2TZVPP basis set (see the Supporting Information). The calculations at M06-2x-D3/Def2TZVPP also suggest the preference for the end-on position (**A**). The optimized geometries of singlet states both at the BP86-D3(BJ) and M06-2x-D3 levels show that the N_2 does not bind to the central Ni(II) center and instead stays aloft within the cavity of the complex at a distance of 3.55 Å from the central Ni(II) (Ni^C) and 3.03−3.54 Å from the two terminal Ni atoms (Ni^T). Figure 1 shows that one of the N atoms of N_2 is significantly close to the left-sided terminal Ni(II) center (3.03 Å), suggesting a slightly higher preference for the terminal Ni(II) center over the central Ni(II) center. The distance between the two terminal Ni atoms, Ni^T-Ni^T (Scheme 2), in the singlet-state optimized structure is 5.22 Å (gas phase) and 5.09 Å (THF), which is slightly longer than the Ni^T-Ni^T distance of 4.90 Å in the experimentally reported[39] crystal structure of the original dianionic Ni_3S_8 complex $[(LS_2)_4Ni(II)_3^{2-}$; Scheme 2, left] containing H-bonded ($LS_2\cdots H-O-H$) water molecules inside the cavity. This implies the slight widening (0.19 Å in THF) of the cavity to facilitate the interaction of N_2. The bridging sulfur (S^B) atoms of the ligand (LS_2^{2-}) are at a 2.20 Å distance from the central Ni(II) (Ni^C) and 2.25−2.27 Å from the two terminal Ni atoms (Ni^T), while the terminal sulfur atoms (S^T) are at a distance of 2.20−2.21 Å from the terminal Ni atoms (Ni^T) (Figure 1). The values correlated well with the experimental values of 2.18−2.20 Å for Ni^C-S^B, 2.23−2.26 Å for Ni^T-S^B, and 2.18−2.21 Å for Ni^T-S^T in the original N_3S_8 cluster.[39] Referring to Figures 1 and S1, the values calculated at BP86-D3(BJ)/Def2TZVPP matched well with the experimental values compared to those calculated at M06-2x-D3/Def2TZVPP. Hence, we further report only the values calculated at the BP86-D3(BJ) level. The authors showed that the Ni_3S_8 complex under a N_2 atmosphere electrocatalytically reduced N_2 at −2.35 V in the presence of a proton source (PhOH) representing the nitrogen reduction reaction (NRR). We attempted to optimize the dianionic and diamagnetic $(Ni_3S_8)N_2$ complex $[(Ni_3S_8)N_2$ (**1**) + $e^- \rightarrow$ **2** or **3**] as a radical anion by adding one electron. This represents one-electron reduction in both end-on and side-on modes of N_2 binding to the central Ni atom (**A and B**). To our surprise, the optimization in the end-on fashion resulted in a geometry (Figure 1 and Schemes 2 and 3) with N_2 bonded to central Ni^C (complex **2**), while the optimization in the side-on fashion resulted in N_2 bonded to one of the terminal Ni^T atoms (complex **3**) rather than the central Ni as shown in Scheme 2 in the gas phase. However, the optimization of complex **3** in THF did not lead to N_2 binding to the terminal Ni and instead, it stayed in the cavity, similar to complex **1**. The N_2 binding to the original Ni_3S_8 complex occurs only under the electrochemically reduced condition, which is analogous to the nitrogenase FeMoco cofactor. Under the resting state of the nitrogenase enzyme, the FeMoco cofactor does not bind to N_2 and rather binds only under reduced conditions.[1−3,5] Our calculations suggest that the cavity further expands on the direct binding of N_2 with Ni, as shown by the Ni^T-Ni^T distances of 5.84 Å (gas) and 5.81 Å (THF) in complex **2** and 6.16 Å in complex **3** (gas). $Ni(I)^C$ of **2** is 0.72 Å above the S_4 plane, and the $Ni(I)^C-S$ bond lengths in **2** significantly increase, whereas $Ni(I)^T$ of **3** is 0.20 Å above the S_4 plane, and the Ni−S distances around $Ni(I)^T$ of **3** increase slightly. Energetically, one-electron reduction of **1** leading to **2** is favored by −23.1 kcal mol^{-1} (ΔG^{298}) in THF. This is the electron affinity value of **1**. In comparison, the same process is highly endothermic (+117.0 kcal mol^{-1}) in the gas phase, suggesting a favorable stabilizing ion−dipole interaction between the complex and the THF solvent molecules (Scheme S1). The dissociation of N_2 is slightly exothermic for both complexes **2** and **3** and the exothermicity is relatively higher in reduced complex **2** (ΔG^{298} = −13.5 kcal mol^{-1}) than in complex **3** (ΔG^{298} = −1.13 kcal mol^{-1}) in the gas phase. Energetically, complex **3** is relatively more stable than complex **2** by 11.1 kcal mol^{-1} (gas). We have also evaluated the complexes under study for the presence of a multireference character by performing coupled-cluster calculations on the optimized geometries. The calculations showed T1 diagnostics of 0.04, 0.038, and 0.043 for complexes **1**, **2**, and **3**, respectively, revealing the absence of a multireference character.[49]

COMPUTATIONAL METHOD

The above observations made us curious about the nature of the Ni−N_2 bond in such complexes. We have employed charge and energy density methods such as natural bond orbital (NBO), quantum theory of atoms in molecules (QTAIM), and energy decomposition analysis coupled with natural orbitals for chemical valence (EDA−NOCV)[6] methods to study the nature of the Ni−N bond in the gas-phase optimized geometries. The details of the methods are provided in the Supporting Information. The EDA−NOCV method is more appropriate in explaining the nature of the bond as one of the major strengths of the method is its ability to provide the best bonding model to represent the bonding situation in the equilibrium geometry. The EDA−NOCV method involves the decomposition of the intrinsic interaction energy (ΔE_{int}) between two fragments into four energy components as follows

$$\Delta E_{int} = \Delta E_{elstat} + \Delta E_{Pauli} + \Delta E_{orb} + \Delta E_{disp} \quad (1)$$

where the electrostatic term (ΔE_{elstat}) is from the interpenetrating charges of the nuclei of the two fragments that attract the electron cloud of the opposite fragment and the orbital term (ΔE_{orb}) is from the mixing and relaxation of the orbitals, charge transfer, and polarization between the isolated fragments. The dispersion term (ΔE_{disp}) is from the noncovalent interactions and, in particular, weak London forces between the two interacting fragments. While the above three terms constitute attractive forces, the Pauli term (ΔE_{Pauli}) arises due to the repulsion between the same electron spin of the two fragments. All four terms are represented as the difference between the two interacting fragments before and after bond formation. The corresponding deformation electron densities are represented by the direction of the charge flow red → blue. See the Supporting Information for the detailed computational part.

https://doi.org/10.1021/acsomega.1c03715
ACS Omega 2021, 6, 33389−33397

Table 1. EDA−NOCV Results at the BP86-D3(BJ)/TZ2P Level of Ni_3Si_8−N_2 Bonds of $[(Ni_3Si_8)N_2]^{\bullet-}$ Radical Anion Complexes (2 and 3) Using Singly Charged $[Ni_3Si_8]^{\bullet-}$ in the Electronic Doublet State and the Neutral N_2 Fragment Electronic Singlet State as Interacting Fragments[c]

energy	interaction	$[Ni_3Si_8]^{\bullet-}$ (D) + $[N_2]$ (S) end-on (2)	$[Ni_3Si_8]^{\bullet-}$ (D) + $[N_2]$ (S) side-on (3)
ΔE_{int}		−24.0	−13.8
ΔE_{Pauli}		164.2	40.0
ΔE_{disp} [a]		−9.5 (5.0%)	−8.5 (15.8%)
ΔE_{elstat} [b]		−95.0 (50.5%)	−20.8 (38.7%)
ΔE_{orb} [b]		−83.7 (44.5%)	−24.5 (45.5%)
$\Delta E_{orb(1)}$ [b]	Ni_3Si_8−N_2 σ polarization	−26.3 (31.5%)	
	$Ni_3Si_8 \rightarrow N_2$ π back-donation		−16.4 (67.0%)
$\Delta E_{orb(2)}$ [b]	$Ni_3Si_8 \leftarrow N_2$ σ donation	−6.0 (7.1%)	−2.7 (11.0%)
$\Delta E_{orb(3)}$ [b]	$Ni_3Si_8 \rightarrow N_2$ π back-donation	−24.7 (29.5%)	
	$Ni_3Si_8 \rightarrow N_2$ π back-donation		−2.3 (9.4%)
$\Delta E_{orb(4)}$ [b]	$Ni_3Si_8 \rightarrow N_2$ π back-donation	−20.1 (24.0%)	
$\Delta E_{orb(rest)}$ [b]		−6.6 (7.9%)	−3.1 (12.6%)

[a]The values in parentheses show the contribution to the total attractive interaction $\Delta E_{elstat} + \Delta E_{orb} + \Delta E_{disp}$. [b]The values in parentheses show the contribution to the total orbital interaction ΔE_{orb}. [c]Energies are in kcal mol^{-1}.

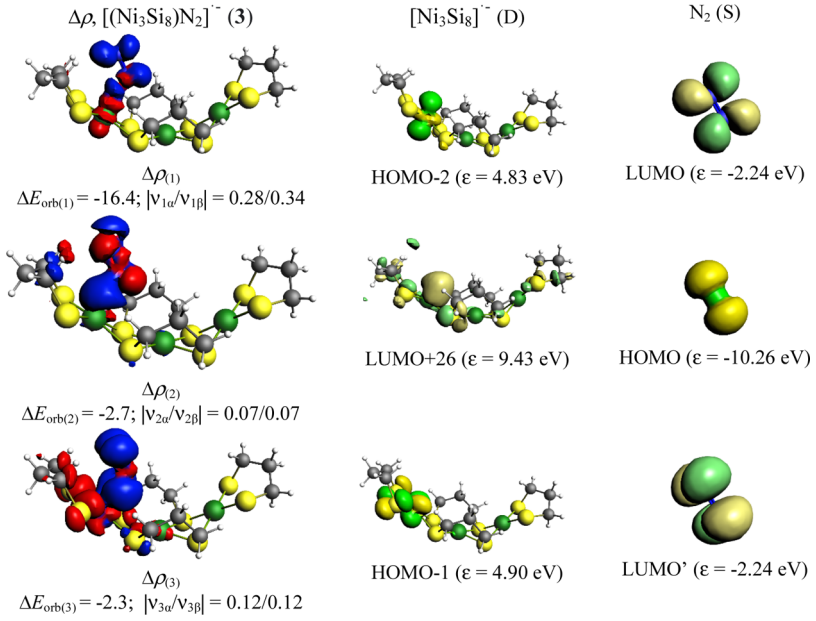

Figure 2. Shape of the deformation densities $\Delta\rho_{(1)-(3)}$ that correspond to $\Delta E_{orb(1)-(3)}$ and the associated MOs of $[(Ni_3Si_8)N_2]^{\bullet-}$ (3) and the fragment orbitals of $[Ni_3Si_8]^{\bullet-}$ in doublet state and N_2 in the singlet state at the BP86-D3(BJ)/TZ2P level. Isosurface values of 0.003 au for $\Delta\rho_{(1)}$ and 0.0003 au for $\Delta\rho_{(2-3)}$. The eigenvalues $|\nu_n|$ give the size of the charge migration in *e*. The direction of the charge flow of the deformation densities is red → blue.

The natural charge from NBO analysis of $(LS_2)_4(N_2)Ni(II)_3^{2-}$ (**1**; $Ni_3S_8N_2$) shows that the total charge on three Ni atoms decreases upon interacting or binding to N_2. The slight decrease in charge in the singlet complex indicates that N_2 interacts with the Ni atoms through the electron clouds, and the decrease in charge is more prominent when N_2 is directly bound to Ni as in reduced complexes **2** and **3** (Figures S5−S8). Similarly, charge dipoles are created on the otherwise neutral N_2 unit upon interacting or binding with Ni, suggesting a charge flow from Ni → N_2 (Table S1). The results suggest a Wiberg bond order of 2.95 for N_2 in the encapsulated resting complex **1**, 2.63 in the reduced trianionic complex **2** with end-on bonded N_2 at the central Ni(I) ion, and 2.79 in the reduced trianionic complex **3** with side-on bonded N_2. The reduced bond orders compared to that of free dinitrogen (3.03) correlated well with the N−N bond lengths in complexes **1**, **2**, and **3** (Figure 1) and indicated the weakening of the N−N bond, which is a crucial step in the activation of N_2. The α-SOMO-2 of the radical anion complex (**3**) with side-on overlap represents the π interaction between the d_{yz} orbital of Ni and the p_y orbital of N_2, while α-SOMO-3 indicates the σ interaction between the d_z^2 orbital of Ni and the p_x orbital of N_2 (Figure S4). The molecular orbital analysis of the alternative reduced complex (**2**) with N_2 bonded to the central Ni in an end-on fashion shows three π interactions represented by α-SOMO-2, α-SOMO-8, and α-SOMO-9 and one σ interaction indicated by α-SOMO-1 (Figure S3). The calculations suggest a Wiberg bond order of 0.70 for the Ni^C−N bond in complex **2** with an electron occupancy of 0.98 e, which is highly polarized toward N (88%), and 0.30 for the Ni−N bond in complex **3** (Table S2). The calculations did not provide bond occupancy for the Ni−N bond in complex **3**. The AIM analysis shows solid bond paths for the Ni−N bond for both complexes **2** and **3** supporting the direct bonding of

https://doi.org/10.1021/acsomega.1c03715
ACS Omega 2021, 6, 33389−33397

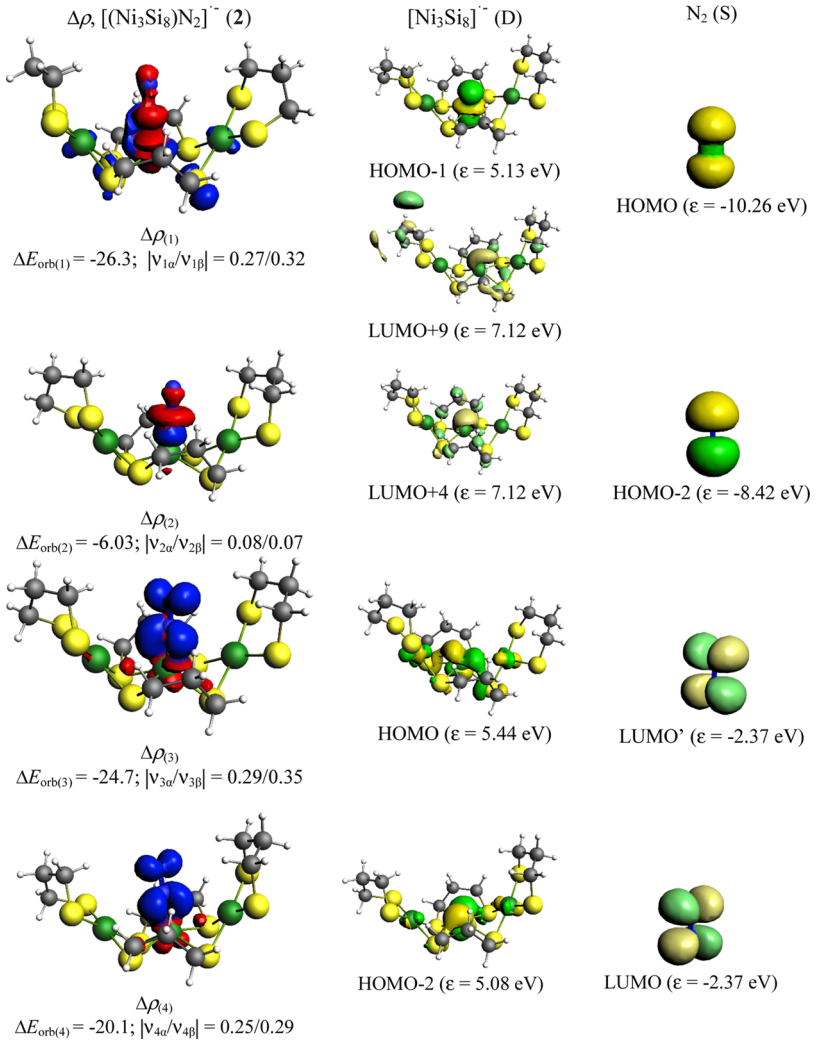

Figure 3. Shape of the deformation densities $\Delta\rho_{(1-4)}$ that correspond to $\Delta E_{orb(1-4)}$ and the associated MOs of $[(Ni_3Si_8)N_2]^{\bullet-}$ (**2**) and the fragment orbitals of $[Ni_3Si_8]^{\bullet-}$ in doublet state and N_2 in the singlet state at the BP86-D3(BJ)/TZ2P level. Isosurface values of 0.003 au for $\Delta\rho_{(1-4)}$. The eigenvalues $|\nu_n|$ give the size of the charge migration in *e*. The direction of the charge flow of the deformation densities is red → blue.

N_2 with Ni (Figure S10). The calculations suggest considerable electron density (ρ_r) at (3, −1) bond critical point (BCP) for complex **2** and a very low electron density at BCP for complex **3** (Table S3). The difference in electron densities at BCPs can be related to shorter and longer Ni−N bond lengths in complexes **2** and **3**, respectively (Figure 1).

We have considered the trianionic reduced Ni_3S_8 fragment in doublet state and the neutral N_2 fragment in singlet state for the EDA−NOCV method to give the best bonding description. The isomeric reduced complex **2** shows a higher intrinsic interaction (24.0 kcal mol^{-1}) than complex **3** (13.8 kcal mol^{-1}), due to an increase in electrostatic contribution and a slight reduction in the orbital contribution of complex **2** relative to that of complex **3** (Table 1). The low intrinsic interaction of the reduced complex **3** (Table 1) correlates well with the long Ni−N bond length (2.447 Å) (Figure 1). The total orbital interactions contribute a major 45.5% to the total attractive interactions, while the electrostatic interactions contribute 38.7%. The dispersion interactions also play a major role in stabilizing the Ni−N bond by contributing not-very-less 15.8% of total attractive interactions. While the electrostatic contributions in **2** provide 50.5% of the total attractive interactions, the orbital interactions contribute 44.5% and the contribution of dispersion interactions is rather small (5.0%). Based on the abovementioned contributions, it can be inferred that the Ni−N bond is slightly more covalent in complex **3**, whereas it is slightly more electrostatic in complex **2** (Table 1). The EDA−NOCV results of complex **2** optimized in THF are almost similar to calculations on the gas-phase optimized geometry with a minor difference of around 2 kcal mol^{-1} lower than the gas-phase calculations (Table S4).

The pairwise breakdown of total orbital interactions provides further insight into the nature of the bonding (Table 1). The deformation densities and associated molecular orbitals of the fragments, as shown in Figures 2 and 3, illustrate the type of interactions and the direction of charge flow from red → blue. The first orbital term $\Delta E_{orb(1)}$ of complex **3** represents π back-donation from the d_z^2 orbital of Ni into the vacant $\pi(p_x)^*$ orbital of N_2 ($d_z^2(Ni) \rightarrow \pi_{N2}^*$) and contributes 67% of the total orbital interactions. The second orbital term $\Delta E_{orb(2)}$ indicates σ electron donation from ($3\sigma_g^+$) HOMO of N_2 into the high-lying vacant orbital of Ni ($N_2 \rightarrow$ Ni) contributing 11% to the total orbital interactions, whereas the third orbital term $\Delta E_{orb(3)}$ represents π back-donation from the d_{yz} orbital of Ni into the vacant LUMO' $\pi(p_y)^*$ orbital of N_2 ($d_{yz}(Ni) \rightarrow \pi_{N2}^*$), which contributes 9.4% to the total orbital

https://doi.org/10.1021/acsomega.1c03715
ACS Omega 2021, 6, 33389−33397

Scheme 4. Most Plausible Mechanism for the N_2 Binding of the Ni_3S_8 Dianionic Complex under Electrochemical Reduced Conditions $[Ni_3S_8 + N_2 \rightarrow 1 + e^- \rightarrow 2/3 + e^- \rightarrow 4]$[a]

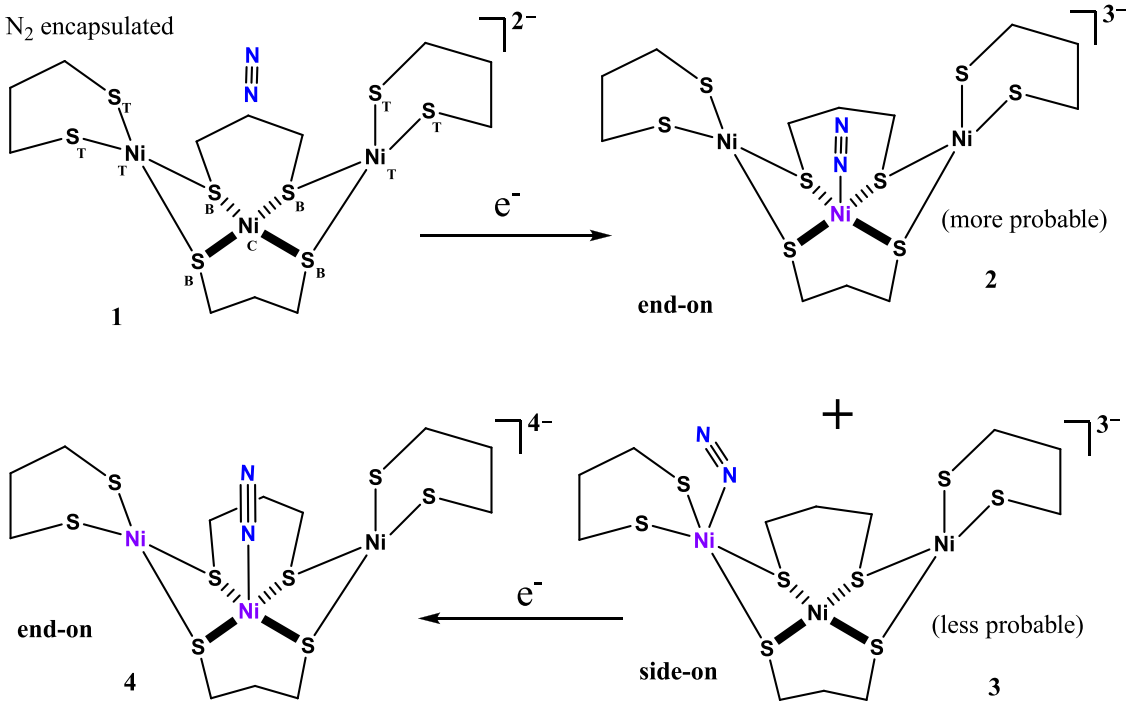

[a]Violet Ni atoms are Ni(I).

interactions. Note that the isosurface values for $\Delta E_{orb(2\text{-}3)}$ are smaller than those of $\Delta E_{orb(1)}$ because otherwise, the minor contributions of the metal atomic orbitals would not be visible (Figure 2). The π back-donations from metal orbitals (Ni → N_2) are significantly stronger than σ donation from N_2 to Ni (N_2 → Ni) in complex **3**. The bent orientation of N_2 in complex **3** makes the π donation possible from Ni → N_2.

The pairwise breakdown of orbital interactions in complex **2** reveals that the first orbital term $\Delta E_{orb(1)}$ denotes σ polarization between the d_{z^2} orbital of Ni and the ($3\sigma_g^+$) HOMO of N_2, while the second orbital term $\Delta E_{orb(2)}$ represents σ electron donation from the sigma (ungerade) orbital of N_2 into the LUMO + 4 orbital of Ni, together contributing 38.6% to the total orbital interactions (Figure 3). Whereas the third $\Delta E_{orb(3)}$ and fourth orbital terms $\Delta E_{orb(4)}$ represent π back-donations from d_{xz} and d_{yz} orbitals of Ni into vacant $\pi(p_y)^*$ and $\pi(p_x)^*$ orbitals of N_2, respectively, together contributing 53.5% of the total orbital interactions. The π back-donations from metal orbitals are stronger than those of σ donations from N_2 in complex **2** and is in good agreement with the bonding analysis of M−N bonds in matrix-isolated triplet $M(N_2)_8$ (M = Ca, Sr, Ba) complexes where N−N bonds are dominated by $[M(d_\pi)] \rightarrow (N_2)_8$ π back-donations from metal orbitals.[30] The stronger π back-donations in complexes **2** and **3** agree well with the charge distribution and reduced Wiberg bond orders from NBO analysis. The deformation densities correlated well with the MOs of complexes **2** and **3**.

Our further calculations suggest that the proton on the N_2 unit of **2** or **3** species jumps to one of the S^T atoms with the dissociation of N_2 from the Ni center. Hence, it is proposed that further reduction intermediate of **2** or **3** species is inferred, leading to the formation of a doubly reduced tetraionic complex **4** with two Ni(I) centers (one Ni^T and Ni^C).

CONCLUSIONS

In conclusion, we carried out quantum chemical calculations on the U-shaped sulfur-bridged dianionic diamagnetic Ni_3S_8 complex to understand the nature of N_2 binding under electrochemical conditions. The calculations suggest that the encapsulation of one N_2 molecule in the cavity is energetically favorable. The left-to-right arm length of the U-shape complex changes on N_2 encapsulation. The binding of N_2 at the triplet state of the Ni_3S_8 complex costs 30 kcal mol^{-1}, which is not feasible under the resting state of this complex. Under electrochemical conditions, N_2 can bind either at the central Ni(I) (**2**) or terminal Ni(I) (**3**) ion at −2.40 V in the presence of PhOH. The Wiberg bond order decreases from 3.03 in free N_2 to 2.95 in N_2-encapsulated resting complex **1**, 2.63 in reduced trianionic complex **2** with end-on bonded N_2 at the central Ni(I) ion, and 2.79 in reduced trianionic complex **3** with side-on bonded N_2. The Ni−N distance is significantly shorter in **2** than in **3**, and the overall Ni−N interaction energy is higher in **2** (with end-on bonded N_2) than in **3** (with side-on bonded N_2). Complex **2** shows higher electrostatic contribution and a slight reduction in the orbital contribution relative to that of complex **3**. However, the magnitude of the orbital interaction energy is higher in **2** than that of **3**. The EDA−NOCV results reveal that the Ni−N bond is slightly more covalent in complex **3**, whereas it is slightly more electrostatic in complex **2**. Additional calculation shows that the protonation of **2**/**3** leads to the dissociation of the N_2 molecule from the reduced complex, and hence, it is suggested that the tetra-anionic form of the Ni_3S_8 complex is more likely (Scheme 4) to undergo protonation toward the electrochemical formation of N_2H_4 either in a "distal" or in an "alternating" pathway.[1,15,23] In both the complexes, π back-donation from nickel to N_2 (M → N_2) is much stronger than

https://doi.org/10.1021/acsomega.1c03715
ACS Omega 2021, 6, 33389−33397

dinitrogen-to-nickel ($N_2 \rightarrow M$) σ-donation, although Yamabe et al. suggested the opposite 4 decades ago.[50] Previously, only one paramagnetic Ni-containing zeolite has been studied by ETS−NOCV toward end-on O_2 binding.[51] The EDA−NOCV analysis reveals the stability of complex **2** over complex **3**. Energetically, one-electron reduction of **1** leading to **2** is also favored by −23.1 kcal mol^{-1} (ΔG^{298}) in THF.

■ ASSOCIATED CONTENT

Supporting Information

The Supporting Information is available free of charge at https://pubs.acs.org/doi/10.1021/acsomega.1c03715.

Computational methods; NBO results; molecular orbital pictures; Laplacian contour plots; schemes representing energetics; and optimized coordinates (PDF)

■ AUTHOR INFORMATION

Corresponding Author

Kartik Chandra Mondal − *Department of Chemistry, Indian Institute of Technology Madras, Chennai 600036, India;* orcid.org/0000-0002-5830-3608; Email: csdkartik@iitm.ac.in

Author

Sai Manoj N. V. T. Gorantla − *Department of Chemistry, Indian Institute of Technology Madras, Chennai 600036, India;* orcid.org/0000-0001-7315-6354

Complete contact information is available at: https://pubs.acs.org/10.1021/acsomega.1c03715

Notes

The authors declare no competing financial interest.

■ ACKNOWLEDGMENTS

The authors thank Prof. Gernot Frenking and Prof. K.M.S for providing computational facilities. S.M. also thanks Dr. S. Pan and CSIR for SRF. K.C.M. thanks SERB for the ECR grant (ECR/2016/000890) and IIT Madras for the seed grant.

■ REFERENCES

(1) Hoffman, B. M.; Dean, D. R.; Seefeldt, L. C. Climbing Nitrogenase: Toward a Mechanism of Enzymatic Nitrogen Fixation. *Acc. Chem. Res.* **2009**, *42*, 609−619.

(2) Crossland, J. L.; Tyler, D. R. Iron−dinitrogen coordination chemistry: Dinitrogen activation and reactivity. *Coord. Chem. Rev.* **2010**, *254*, 1883−1894.

(3) Rittle, J.; Peters, J. C. Fe−N_2/CO complexes that model a possible role for the interstitial C atom of FeMo-cofactor (FeMoco). *Proc. Natl. Acad. Sci. U.S.A.* **2013**, *110*, 15898.

(4) McWilliams, S. F.; Broere, D. L. J.; Halliday, C. J. V.; Bhutto, S. M.; Mercado, B. Q.; Holland, P. L. Coupling dinitrogen and hydrocarbons through aryl migration. *Nature* **2020**, *584*, 221.

(5) Cai, R.; Minteer, S. D. Nitrogenase Bioelectrocatalysis: From Understanding Electron-Transfer Mechanisms to Energy Applications. *ACS Energy Lett.* **2018**, *3*, 2736.

(6) (a) Zhao, L.; Pan, S.; Holzmann, N.; Schwerdtfeger, P.; Frenking, G. Chemical Bonding and Bonding Models of Main-Group Compounds. *Chem. Rev.* **2019**, *119*, 8781. (b) Jerabek, P.; Frenking, G. Comparative Bonding Analysis of N_2 and P_2 versus Tetrahedral N_4 and P_4. *Theor. Chem. Acc.* **2014**, *133*, No. 1447.

(7) Choudhury, S. B.; Lee, J. W.; Davidson, G.; Yim, Y. I.; Bose, K.; Sharma, M. L.; Kang, S. O.; Cabelli, D. E.; Maroney, M. J. Examination of the Nickel Site Structure and Reaction Mechanism in Streptomyces seoulensis Superoxide Dismutase. *Biochemistry* **1999**, *38*, 3744.

(8) Barondeau, D. P.; Kassmann, C. J.; Bruns, C. K.; Tainer, J. A.; Getzoff, E. D. Nickel Superoxide Dismutase Structure and Mechanism. *Biochemistry* **2004**, *43*, 8038.

(9) Ogata, H.; Nishikawa, K.; Lubitz, W. Hydrogens Detected by Subatomic Resolution Protein Crystallography in a [NiFe] Hydrogenase. *Nature* **2015**, *520*, 571.

(10) Bruschi, M.; Tiberti, M.; Guerra, A.; De Gioia, L. Disclosure of Key Stereoelectronic Factors for Efficient H_2 Binding and Cleavage in the Active Site of [NiFe]-Hydrogenases. *J. Am. Chem. Soc.* **2014**, *136*, 1803.

(11) Minteer, S. D.; Christopher, P.; Linic, S. Recent Developments in Nitrogen Reduction Catalysts: A Virtual Issue. *ACS Energy Lett.* **2019**, *4*, 163−166.

(12) Matson, B. D.; Peters, J. C. Fe-Mediated HER vs N_2RR: Exploring Factors That Contribute to Selectivity in $P_3^EFe(N_2)$ (E = B, Si, C) Catalyst Model Systems. *ACS Catal.* **2018**, *8*, 1448.

(13) Thompson, N. B.; Green, M. T.; Peters, J. C. Nitrogen Fixation via a Terminal Fe(IV) Nitride. *J. Am. Chem. Soc.* **2017**, *139*, 15312.

(14) Lee, Y.; Sloane, F. T.; Blondin, G.; Abboud, K. A.; García-Serres, R.; Murray, L. J. Dinitrogen Activation upon Reduction of a Triiron(II) Complex. *Angew. Chem., Int. Ed.* **2015**, *54*, 1499.

(15) Ćorić, I.; Holland, P. L. Insight into the Iron−Molybdenum Cofactor of Nitrogenase from Synthetic Iron Complexes with Sulfur, Carbon, and Hydride Ligands. *J. Am. Chem. Soc.* **2016**, *138*, 7200.

(16) Wickramasinghe, L. A.; Ogawa, T.; Schrock, R. R.; Müller, P. Reduction of Dinitrogen to Ammonia Catalyzed by Molybdenum Diamido Complexes. *J. Am. Chem. Soc.* **2017**, *139*, 9132.

(17) Fajardo, J., Jr.; Peters, J. C. Catalytic Nitrogen-to-Ammonia Conversion by Osmium and Ruthenium Complexes. *J. Am. Chem. Soc.* **2017**, *139*, 16105.

(18) Lindley, B. M.; van Alten, R. S.; Finger, M.; Schendzielorz, F.; Wurtele, C.; Miller, A. J. M.; Siewert, I.; Schneider, S. Mechanism of Chemical and Electrochemical N_2 Splitting by a Rhenium Pincer Complex. *J. Am. Chem. Soc.* **2018**, *140*, 7922.

(19) Sekiguchi, Y.; Arashiba, K.; Tanaka, H.; Eizawa, A.; Nakajima, K.; Yoshizawa, K.; Nishibayashi, Y. Catalytic Reduction of Molecular Dinitrogen to Ammonia and Hydrazine Using Vanadium Complexes. *Angew. Chem., Int. Ed.* **2018**, *57*, 9064.

(20) Yao, Y.; Zhu, S.; Wang, H.; Li, H.; Shao, M. A Spectroscopic Study on the Nitrogen Electrochemical Reduction Reaction on Gold and Platinum Surfaces. *J. Am. Chem. Soc.* **2018**, *140*, 1496.

(21) Čorić, I.; Mercado, B. Q.; Bill, E.; Vinyard, D. J.; Holland, P. L. Binding of Dinitrogen to an Iron-Sulfur-Carbon Site. *Nature* **2015**, *526*, 96.

(22) Rittle, J.; Peters, J. C. Fe−N_2/CO complexes that model a possible role for the interstitial C atom of FeMo-cofactor (FeMoco). *Proc. Natl. Acad. Sci. U.S.A.* **2013**, *110*, 15898.

(23) Bruch, Q. J.; Connor, G. P.; McMillion, N. D.; Goldman, A. S.; Hasanayn, F.; Holland, P. L.; Miller, A. J. M. Considering Electrocatalytic Ammonia Synthesis via Bimetallic Dinitrogen Cleavage. *ACS Catal.* **2020**, *10*, 10826.

(24) Ung, G.; Peters, J. C. Low-Temperature N_2 Binding to Two-Coordinate L_2Fe^0 Enables Reductive Trapping of $L_2FeN_2^-$ and NH_3 Generation. *Angew. Chem., Int. Ed.* **2015**, *54*, 532.

(25) Mankad, N. P.; Whited, M. T.; Peters, J. C. Terminal Fe^I−N_2 and Fe^{II}···H−C Interactions Supported by Tris(phosphino)silyl Ligands. *Angew. Chem., Int. Ed.* **2007**, *46*, 5768.

(26) Lee, Y.; Mankad, N. P.; Peters, J. C. Triggering N_2 uptake via redox-induced expulsion of coordinated NH_3 and N_2 silylation at trigonal bipyramidal iron. *Nat. Chem.* **2010**, *2*, 558.

(27) Creutz, S. E.; Peters, J. C. Catalytic Reduction of N_2 to NH_3 by an Fe−N_2 Complex Featuring a C-Atom Anchor. *J. Am. Chem. Soc.* **2014**, *136*, 1105.

(28) Légaré, M.-A.; Bélanger-Chabot, G.; Dewhurst, R. D.; Welz, E.; Krummenacher, I.; Engels, B.; Braunschweig, H. Nitrogen fixation and reduction at boron. *Science* **2018**, *359*, 896.

(29) Broere, D. L. J.; Holland, P. L. Boron compounds tackle dinitrogen. *Science* **2018**, *359*, 871.
(30) Wang, Q.; Pan, S.; Lei, S.; Jin, J.; Deng, G.; Wang, G.; Zhao, L.; Zhou, M.; Frenking, G. Octa-Coordinated Alkaline Earth Metal−Dinitrogen Complexes $M(N_2)_8$ (M=Ca, Sr, Ba). *Nat. Commun.* **2019**, *10*, No. 3375.
(31) Hill, P. J.; Doyle, L. R.; Crawford, A. D.; Myers, W. K.; Ashley, A. E. Selective Catalytic Reduction of N_2 to N_2H_4 by a Simple Fe Complex. *J. Am. Chem. Soc.* **2016**, *138*, 13521.
(32) Bazhenova, T. A.; Shilov, A. E. Nitrogen fixation in solution. *Coord. Chem. Rev.* **1995**, *144*, 69.
(33) Kuriyama, S.; Arashiba, K.; Nakajima, K.; Matsuo, Y.; Tanaka, H.; Ishii, K.; Yoshizawa, K.; Nishibayashi, Y. Catalytic transformation of dinitrogen into ammonia and hydrazine by iron-dinitrogen complexes bearing pincer ligand. *Nat. Commun.* **2016**, *7*, No. 12181.
(34) Iwamoto, M.; Akiyama, M.; Aihara, K.; Deguchi, T. Ammonia Synthesis on Wool-Like Au, Pt, Pd, Ag, or Cu Electrode Catalysts in Nonthermal Atmospheric-Pressure Plasma of N_2 and H_2. *ACS Catal.* **2017**, *7*, 6924.
(35) Lindley, B. M.; Appel, A. M.; Krogh-Jespersen, K.; Mayer, J. M.; Miller, A. J. M. Evaluating the Thermodynamics of Electrocatalytic N_2 Reduction in Acetonitrile. *ACS Energy Lett.* **2016**, *1*, 698.
(36) Soloveichik, G. L. Liquid Fuel Cells. *Beilstein J. Nanotechnol.* **2014**, *5*, 1399−1418.
(37) Kohnke, H. Hydrazine Fuel Cells. *Handb. Fuel Cells* 2010, 2−7 DOI: 10.1002/9780470974001.f207053.
(38) Mitchell, M. C.; Rakoff, R. W.; Jobe, T. O.; Sanchez, D. L.; Wilson, D. B. Thermodynamic Analysis of Equations of State for the Monopropellant Hydrazine. *J. Thermophys. Heat Transfer* **2007**, *21*, 243.
(39) Saha, P.; Amanullah, S.; Dey, A. Electrocatalytic Reduction of Nitrogen to Hydrazine Using a Trinuclear Nickel Complex. *J. Am. Chem. Soc.* **2020**, *142*, 17312−17317.
(40) Ziegler, T.; Rauk, A. On the calculation of bonding energies by the Hartree Fock Slater method. *Theor. Chim. Acta* **1977**, *46*, 1.
(41) Mitoraj, M.; Michalak, A. Donor−Acceptor Properties of Ligands from the Natural Orbitals for Chemical Valence. *Organometallics* **2007**, *26*, 6576.
(42) Mitoraj, M.; Michalak, A. Applications of natural orbitals for chemical valence in a description of bonding in conjugated molecules. *J. Mol. Model.* **2008**, *14*, 681.
(43) ADF2017, *SCM, Theoretical Chemistry*; Vrije Universiteit: Amsterdam, The Netherlands. http://www.scm.com.
(44) te Velde, G.; Bickelhaupt, F. M.; Baerends, E. J.; Guerra, C. F.; van Gisbergen, S. J. A.; Snijders, J. G.; Ziegler, T. Chemistry with ADF. *J. Comput. Chem.* **2001**, *22*, 931.
(45) (a) van Lenthe, E.; Baerends, E. J. Optimized Slater-type basis sets for the elements 1−118. *J. Comput. Chem.* **2003**, *24*, 1142. (b) van Lenthe, E.; Baerends, E. J.; Snijders, J. G. Relativistic regular two-component Hamiltonians. *J. Chem. Phys.* **1993**, *99*, 4597.
(46) van Lenthe, E.; Baerends, E. J.; Snijders, J. G. Relativistic total energy using regular approximations. *J. Chem. Phys.* **1994**, *101*, 9783.
(47) (a) Frenking, G.; Bickelhaupt, F. M. *The Chemical Bond 1. Fundamental Aspects of Chemical Bonding*; Wiley-VCH: Weinheim, 2014; Vol. *121*, Chapter: The EDA Perspective of Chemical Bonding. (b) Zhao, L.; von Hopffgarten, M.; Andrada, D. M.; Frenking, G. *WIREs Comput. Mol. Sci.* **2018**, *8*, No. 1345. (c) Zhao, L.; Hermann, M.; Schwarz, W. H. E.; Frenking, G. The Lewis electron-pair bonding model: modern energy decomposition analysis. *Nat. Rev. Chem.* **2019**, *3*, 48. (d) Yang, W.; Krantz, K. E.; Freeman, L. A.; Dickie, D.; Molino, A.; Frenking, G.; Pan, S.; Wilson, D. J. D.; Gilliard, R. J., Jr. Persistent Borafluorene Radicals. *Angew. Chem., Int. Ed.* **2020**, *59*, 3850−3854.
(48) (a) Andrés, J.; Ayers, P. W.; Boto, R. A.; Carbó-Dorca, R.; Chermette, H.; Cioslowski, J.; Contreras-García, J.; Cooper, D. L.; Frenking, G.; Gatti, C.; Heidar-Zadeh, F.; Joubert, L.; Martín Pendás, A.; Matito, E.; Mayer, I.; Misquitta, A. J.; Mo, Y.; Pilmé, J.; Popelier, P. L. A.; Rahm, M.; Ramos-Cordoba, E.; Salvador, P.; Schwarz, W. H. E.; Shahbazian, S.; Silvi, B.; Solà, M.; Szalewicz, K.; Tognetti, V.; Weinhold, F.; Zins, E. L. Nine questions on energy decomposition analysis. *J. Comput. Chem.* **2019**, *40*, 2248.
(49) Jiang, W.; Deyonker, N. J.; Wilson, A. K. Multireference Character for 3d Transition-Metal-Containing Molecules. *J. Chem. Theory Comput.* **2012**, *8*, 460.
(50) Yamabe, T.; Hori, K.; Ninato, T.; Fukui, K. Theoretical Study on the Bonding Nature of Transition-Metal Complexes of Molecular Nitrogen. *Inorg. Chem.* **1980**, *19*, 2154.
(51) Pietrzyk, P.; Podolska, K.; Mazur, T.; Sojka, Z. Heterogeneous Binding of Dioxygen: EPR and DFT Evidence for Side-On Nickel(II)-Superoxo Adduct with Unprecedented Magnetic Structure Hosted in MFI Zeolite. *J. Am. Chem. Soc.* **2011**, *133*, 19931.

https://doi.org/10.1021/acsomega.1c03715
ACS Omega 2021, 6, 33389−33397